Semicomputational calculation of Bragg shift in stratified materials

Benjamin Frey [1,*] Patrick Snyder,[2,†] Klaus Ziock,[3,‡] and Ali Passian [3,§]

[1]*Department of Physics, University of St. Thomas, Saint Paul, Minnesota 55105-1094, USA*
[2]*Department of Physics, University of Illinois Urbana-Champaign, Urbana, Illinois 61801-3003, USA*
[3]*Oak Ridge National Laboratory, Oak Ridge, Tennessee 37831-6123, USA*

The fiber Bragg grating (FBG) may be viewed as a one dimensional photonic band-gap crystal by virtue of the periodic spatial perturbation imposed on the fiber core dielectric material. Similar to media supporting Bloch waves, the engraved weak index modulation, presenting a periodic "potential" to an incoming guided mode photon of the fiber, yields useful spectral properties that have been the basis for sensing applications and emerging quantum squeezing and solitons. The response of an FBG sensor to arbitrary external stimuli represents a multiphysics problem without a known analytical solution despite the growing use of FBGs in classical and quantum sensing and metrology. Here, we study this problem by first presenting a solid mechanics model for the thermal and elastic states of a stratified material. The model considers an embedded optical material domain that represents the Bragg grating, here in the form of an FBG. Using the output of this model, we then compute the optical modes and their temperature- and stress-induced behavior. The developed model is applicable to media of arbitrary shape and composition, including soft matter and materials with nonlinear elasticity and geometric nonlinearity. Finally, we employ the computed surface stress and temperature distributions along the grating to analytically calculate the Bragg shift, which is found to be in reasonable agreement with our experimental measurements.

I. INTRODUCTION

The realization that the Bragg diffraction of radiation, first observed in crystalline materials, may be mimicked in a material in which the index of refraction n can be made periodic, has enabled many forms of sensing applications. For photons of wavelength λ, propagating in an otherwise uniform medium, a modulation of n at a suitable spatial frequency Λ, analogous to the specific arrangement of atoms in a crystal, can induce an interference pattern with useful spectral properties. If the optical medium is the core ($n = n_C$) of an optical fiber, then the system is referred to as a fiber Bragg grating (FBG). By design, the response of a general Bragg grating to a broadband input radiation is a complete reflection in a spectral band (stopband), the width of which is controlled by Λ, the number of periods $m = 0, 1, 2, \ldots, N$, and index variation with coordinate z along the grating between low and high values $n_L \leqslant n_C(z) \leqslant n_H$. The stopband is peaked at the Bragg wavelength λ_B, the shift of which, in response to external stimuli, furnishes the sensor transduction mechanism. This same Bragg grating transduction mechanism is extended to sensing based on an FBG.

The FBGs, while actively receiving new theoretical prospects [1,2] and opportunities for applications [3–7], have already demonstrated their potential as sensitive optical devices capable of measuring environmental parameters such as stress [8,9], strain [10], temperature [11], humidity [12], pressure [13], etc. [14]. Therefore, FBG-based sensors have been used in numerous practical applications, such as structural health monitoring [15,16], laminate crack propagation analysis [17], biomedical applications [18], and intrusion detection [19].

Due to the sensitivity of the FBG parameters to external stimuli, each of these applications presents a unique set of thermo-optomechanical material considerations when designing for an appropriate sensor implementation. These unique material considerations necessitate multiparameter simulations based on multiply coupled partial differential equations (PDEs), as noted in Fig. 1. Furthermore, due to a lack of symmetries, and the presence of symmetry-breaking stress and deformation, these simulations often require a full account of the spatial dimensions. In addition, for emerging studies involving single photons or photon correlations, one may have to invoke quantum optics for proper FBG response. More specifically, to stimulate further interest, the potential relevance of FBGs in quantum optics and quantum sensing may be exemplified via recent work on quantum applications such as photon trapping within an FBG [20], or quantum soliton propagation in an FBG [21], and more recently frequency generation using FBG filters [22].

Despite the above applications, a simulator capable of collectively accounting for the effects of arbitrary stress, strain, temperature, and photonic configurations on the response of a general optical Bragg grating sensor is currently not

———————
*ben.frey@stthomas.edu
†psnyder@illinois.edu
‡ziockk@ornl.gov
§passianan@ornl.gov

$$\begin{cases} \boldsymbol{v} \cdot \boldsymbol{\nabla} T - \boldsymbol{\nabla} \cdot (k_\Omega \boldsymbol{\nabla} T - \boldsymbol{\Phi}_r) / \rho_\Omega C_\Omega + T_t = \sum_i Q_i & \Omega_C, \cdots, \Omega_\infty \\ \boldsymbol{\nabla} \cdot \boldsymbol{\sigma} + \rho_\Omega \boldsymbol{f} = \rho_\Omega \boldsymbol{u}_{tt}, & \Omega_C, \cdots, \Omega_\infty \\ \boldsymbol{\sigma} = \boldsymbol{C} : \boldsymbol{\varepsilon}, \ 2\boldsymbol{\varepsilon} = \boldsymbol{\nabla}\boldsymbol{u} + (\boldsymbol{\nabla}\boldsymbol{u})^T & \Omega_C, \cdots, \Omega_\infty \\ \boldsymbol{\nabla} \times \boldsymbol{\nabla} \times \boldsymbol{E} = k_0 \epsilon_\Omega \boldsymbol{E} & \Omega_C, \Omega_{CL}, \Omega_J \\ \boldsymbol{n} \times (\boldsymbol{E}_+ - \boldsymbol{E}_-) = 0 & \partial\Omega_{C,CL}, \partial\Omega_{CL,J} \\ \boldsymbol{n} \times \boldsymbol{H} = 0 & \partial\Omega_{J,H} \\ -\boldsymbol{n} \cdot (k_\Omega \boldsymbol{\nabla} T) = 0, \ \boldsymbol{\sigma} \cdot \boldsymbol{e}_y = \boldsymbol{f} & \partial\Omega_{H,\infty} \\ \boldsymbol{u}_- = \boldsymbol{u}_+, \ T_- = T_+ & \partial\Omega_{C,CL}, \cdots, \partial\Omega_{H,\infty} \\ \boldsymbol{u} = 0 & \partial\Omega_\infty \end{cases}$$
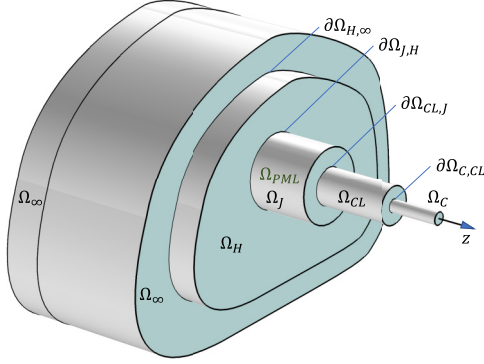

FIG. 1. A segment of the proposed computational domain, subdomains Ω, and boundaries $\partial\Omega$ for modeling an arbitrarily embedded FBG in a stratified medium. The subscripts on Ω and $\partial\Omega$ are defined as C (core), CL (cladding), J (jacket), H (host), and ∞ (infinite domain). When solving the optical problem, subdomain Ω_J becomes a perfectly matched layer (Ω_{PML}). The general forms of the PDEs to be solved and the assumed boundary conditions are annotated, where the dependent variables T, $\boldsymbol{u}$, and $\boldsymbol{E}$, are temperature, displacement field, and electric field, respectively, while $\boldsymbol{H}$, $\boldsymbol{\Phi}_r$, and $\boldsymbol{v}$ are magnetic field, radiative heat flux, and the velocity vector of the subdomain translational motion, respectively. The terms Q_i, $i = 1, 2, \dots$ specify various sources including thermoelastic effect.

available. Whereas, decoupled mechanical, thermal, and photonic subproblems may each be treated to various degrees of satisfaction, solving the coupled problem poses significant scale-related challenges hampering the full exploitation of FBG sensing abilities [23]. For $\lambda = 1.55 \ \mu$m, to achieve sufficient sensitivity (e.g., required resolution for registering a shift in λ_B), typically $\Lambda \propto 0.5 \ \mu$m is used. For a 1-mm-long sensor, a grating will have about 2000 periods (with each period corresponding to a transition from a t_H thick layer of n_H to a t_L thick layer with n_L), making modeling within the wave propagation (or full-wave) regime challenging. This is valid in both transient and harmonic regimes. Numerical techniques such as the finite element method (FEM) and the finite difference time domain (FDTD) method are fully capable of accurately simulating field properties over a few grating periods for moderate processing costs [24]. However, treating thousands of periods under ambient degrees of freedom remains a challenge. Analysis based on mode expansion and coupled-mode theories offer only limited capabilities for predicting the properties of the relevant modes for FBG use cases in which the grating domain is severely warped. Limited semi-computational methods have been reported for determining curvature-induced and spirally coupled modes of cylindrical domains with uniform (no core modulation) n, typically in an attempt to predict curvature-induced mode field distributions and confinement [25]. However, these approaches consider

only either the waveguide geometric effects or the mechanical effects, but not both. Other approaches for computing light propagation in complex optical systems include modeling within geometric optics using advanced (i.e., accounting for phase modulations and interference) ray tracing algorithms, which generally offers an advantage for large length-scale simulations [26], even for cases involving interference, which requires ray phase information. However, as will be discussed, Bragg shifts may be calculated only for specific waveguide geometries.

In an attempt to develop a simulation environment for FBGs, Pereira *et al.* [27] reported a PYTHON program (FBG_SiMul V1.0) for calculating the spectral shift of an FBG that can accommodate multiple serial gratings. This simulator is based on optical coupled mode theory, allowing for the study of transmittance and reflectance through a modal transfer matrix method implementation. Here, we extend this simulator to allow cases in which temperature T can vary. However, the underlying equations currently only consider the temperature of the grating medium and as such one has to supply a T-dependent stress computation to account for realistic birefringence and mode shift contribution. Nevertheless, as shown below, the extended simulator version (FBG-SimPlus V1.0) [28] reported here, emulates Bragg shift dependence on T reasonably well without an additional T-dependent stress computation, for small T changes. The new program is made available at a public code repository for use in cases where the contribution of small thermal variations to strain, stress, and optical properties is important when simulating the response of an FBG.

Our presentation is organized as follows. Section II presents the proposed model geometry and analytical formulation of the equations to be solved. Here, the various optical, thermal, and mechanical effects are considered in the calculation of the Bragg shift. First, we computationally obtain the temperature and stress distribution in an arbitrary region of an embedding medium along the surfaces of an embedded grating. The results are then used in a modified analytical formulation of FBG spectral shift. In doing so, we extend the simulation platform of Pereira *et al.* Two scenarios will generate output, referred to as "computational results" and "emulated results." In the former, T is obtained by solving the diffusion equation within the FE model, whereas in the latter, T is assumed fixed in the FE model, that is, no heat equation solved, but thermal effects are emulated within the FBG simulator. In Sec. III, we present our experimental measurements using an FBG under the conditions of stress and temperature. The computational results are compared with experimental data using a single-mode step-index FBG sensor. Section IV provides our concluding remarks. Due to the multiphysics nature of the problem, and for the sake of completeness, we maintain a slightly detailed presentation.

II. BRAGG SHIFT CALCULATION

A. Model geometry

We are concerned with thermophysical processes that change the optical, mechanical, and geometric properties of the FBG system; in particular, in the core-cladding region

of the fiber. To set up our model, we propose the computational domain shown in Fig. 1, and review the general forms of the relevant PDEs, as annotated. The solution outputs of this model are to provide stress, strain, and initial temperature distributions. More specifically, consider an optical fiber embedded in an arbitrary host or matrix medium, as shown in Fig. 1. In what follows, for tensor quantities, we will use the permutations of the spatial coordinates labeled as $i, j \in \{1, 2, 3\}$, or $\in \{x, y, z\}$. To model the proper material stratification, the computational domain Ω is written as the following union of subdomains:

$$\Omega \triangleq \Omega_C \cup \Omega_{CL} \cup \Omega_J \cup \Omega_H \cup \Omega_\infty,$$

making up (1) three concentric cylindrical regions of radii R_C, R_{CL}, and R_J dedicated to the core (Ω_C), the cladding (Ω_{CL}), and the jacket (Ω_J), respectively; (2) a domain of an arbitrary shape dedicated to the host (Ω_H); and (3) an outer domain (Ω_∞) with proper scaling properties to allow simulation of an infinite domain. Here, the union of the subdomains above is assumed to imply perfect bonding of the two materials at each side of any given interface $\partial\Omega$, an assumption that may be subject to further discussion for highly dissimilar materials [29], as noted below. The undeformed cylindrical axis coincides with the z axis, as indicated in Fig. 1. In the present simulation, we assume $R_C = 5$ μm for a typical single-mode fiber (SMF) core, $R_{CL} = 62.5$ μm, and $R_J = 75$ μm, while all other parameters will be defined in the following sections.

Having geometrically defined the computational domain Ω, we now aim to model the processes that may shift the wavelength at which the FBG reflects. These effects change the spectral shape of the reflection, the peak of which is here referred to as the Bragg shift λ_B. To determine the physical changes of the FBG, we need to calculate the stress distribution for arbitrary external stimuli, as described by the subdomain PDEs and proper conditions applied to ith boundary $\partial\Omega_i$, defined as the intersection in Fig. 1:

$$\partial\Omega_i \triangleq \Omega_i \cap \Omega_{i+1}.$$

No specific morphological constraints are assumed for the interfaces $\partial\Omega_i$ which are taken to be smooth. Roughness may, however, be modeled [30], e.g., by topographically approximating a boundary as a surface of a given fractal dimension and spatial frequency.

B. Computational solid mechanics

To obtain the stress, strain, and the deformation states of the modeled material system of Fig. 1, we aim to describe the system within the framework of continuum mechanics. The resulting PDEs are then solved numerically using FEM. We begin by considering the general deformation state of the embedded FBG material system. Denoting the displacement field by $\boldsymbol{u}(x, y, z) = (u, v, w)$, the (linear) strain tensor is written as $2\boldsymbol{\varepsilon}(x, y, z) = \nabla\boldsymbol{u} + (\nabla\boldsymbol{u})^T$, which is valid for small displacements but is modified for large displacements (as geometric nonlinearity grows). The distribution of stress $\boldsymbol{\sigma}$ on the fiber core surface can be obtained from the deformation induced by an arbitrary applied force $\boldsymbol{f} = f(\boldsymbol{r})$ somewhere in the host, representing external stimuli of an FBG sensor. Within the linear elasticity regime, in a general basis $\boldsymbol{e}^k$ ($k = 1, 2, 3$),

TABLE I. Model subdomain material properties under the assumption of no external forces, i.e., $\boldsymbol{f} = 0$ and at initial (room) temperatures $T = T_i$.

Subdomain	Material	ρ [kg/m^3]	E [GPa]	ν
Ω_C	Ge-doped SiO$_2$	2250	75	0.20
Ω_{CL}	SiO$_2$	2203	70	0.16
Ω_J	Acrylate	1190	3.2	0.35
Ω_H	Si	2329	170	0.28
Ω_∞	Matched	Matched	Matched	Matched

with $\boldsymbol{e}_j \cdot \boldsymbol{e}^i = \delta_j^i$, the force per deformed area or stress of the system given by the (Cauchy) stress tensor $\sigma_{ij}\boldsymbol{e}_i\boldsymbol{e}_j$ and (elastic) strain tensor $\varepsilon_{kl}\boldsymbol{e}_k\boldsymbol{e}_l$ are connected via the fourth-order stiffness tensor $C_{ijkl}\boldsymbol{e}_i\boldsymbol{e}_j\boldsymbol{e}_k\boldsymbol{e}_l$ of the material of a given domain, and one writes $\boldsymbol{\sigma} = \boldsymbol{C} : \boldsymbol{\varepsilon}$, where the double contraction operator (:) denotes summing over two indices, here k and l, thus

$$(\boldsymbol{C} : \boldsymbol{\varepsilon})_{ij} = \sum_k \sum_l C_{ijkl}\varepsilon_{kl}.$$

The components of $\boldsymbol{C}$ depend on the specific materials modeled for each subdomain in Fig. 1.

In the present model, the subdomains $\Omega_{C,...,\infty}$ are occupied according to Table I, where the outer layers, subdomains Ω_∞, emulating infinite domain boundary conditions, are composed of materials matching the corresponding materials making up the adjacent subdomains. The constitutive tensor $\boldsymbol{C} = \boldsymbol{C}(E_\Omega, \nu_\Omega) = \boldsymbol{C}_\Omega$, with E_Ω, and ν_Ω being Young's modulus and the Poisson ratio of each subdomain, respectively, take a simpler (isotropic) form for material choices considered here. The stress $\boldsymbol{\sigma}$ is here obtained by first solving for the unknown functions $\boldsymbol{u}$ using the (Navier) equation of motion: $\nabla \cdot \boldsymbol{\sigma} + \rho_\Omega\boldsymbol{f} = \rho_\Omega\boldsymbol{u}_{tt}$ over each subdomain Ω with mass density ρ_Ω, as shown in Fig. 1. The densities ρ_Ω, and other properties considered here, are summarized in Table I.

We choose the upper boundaries for application of a surface force $\boldsymbol{f} = \boldsymbol{\sigma} \cdot \boldsymbol{n}$, which can be implemented to be stationary or transient, but otherwise arbitrary. Here, a stationary force $\boldsymbol{f} = \boldsymbol{\sigma} \cdot (-\boldsymbol{e}_y)$, applied to the outer boundary of the host $\partial\Omega_{H,\infty}$, suffices (see Fig. 1). Therefore, in our sensing use case, stationary fields are sought, consequently, $\boldsymbol{u}_{tt} = 0$. In solving for $\boldsymbol{u}$, we apply the boundary condition $\boldsymbol{u} = \boldsymbol{0}$ to the outer surfaces of the infinite element domains Ω_∞ to help with the solution stability by suppressing rigid body motion. All other interfaces $\partial\Omega$ satisfy continuity in displacement $\boldsymbol{u}$, as annotated in Fig. 1. Depending on how dissimilar the two materials are, the traction can also be continuous [29].

How the external stimuli, here emulated as an applied force, derives displacement and stress within the subdomains, can be described using the weak formulation (Galerkin method) of the PDEs, which is implemented in the FEM rather than the continuous operator (i.e., strong) form above and annotated in Fig. 1. In the subdomains, we have $\boldsymbol{f} = 0$, while on the $y > 0$ segment of $\partial\Omega_{H,\infty}$, we use $\boldsymbol{f} \neq 0$. In the weak formulation, the Navier equation is multiplied with a weight (or test) function and integrated over Ω, which after invoking Green's identity (or divergence theorem, also equivalent to integration by parts), connects the subdomains with the
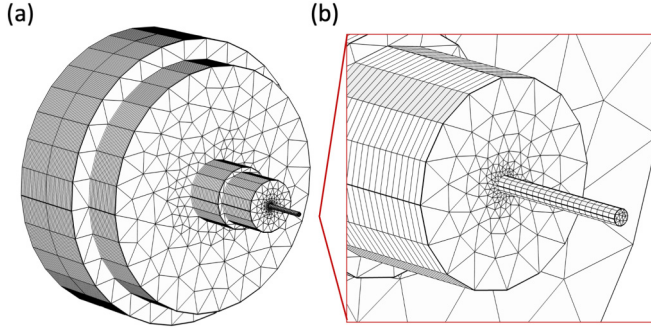
FIG. 2. (a) Meshing of the subdomains for the computational analysis of the mechanical and thermal states of the stratified medium. The mesh shown hides specific outer subdomains for display of inner subdomains and boundary meshing patterns. For the subdomains with a free triangular mesh, a maximum element size of 70 μm and a minimum mesh element size of 12.6 μm were employed for subdomains Ω_J, Ω_H, and Ω_∞. A denser mesh was employed for providing more resolute FEM analysis for Ω_C and Ω_{CL}; here a free triangular mesh of 38.5 μm maximum element size and 2.8 μm minimum element size were used. All boundaries were meshed with a swept distributed pattern of spacing 1 μm. (b) Magnified core and cladding mesh.

boundaries as

$$\int_\Omega \boldsymbol{\sigma} : (\nabla \tilde{\boldsymbol{v}}) \, d\Omega = \int_{\partial \Omega_{H,\infty}} \boldsymbol{f} \cdot \tilde{\boldsymbol{v}} \, dS,$$

where $\tilde{\boldsymbol{v}}$ is the test function of the displacement vector. To properly resolve the features, a $L = 200$-μm-long segment of the subdomains was meshed as shown in Fig. 2. The results are shown in Fig. 3. To assess the mechanical response of the subdomains, solutions were also obtained for the configurations listed in Table II. Since FBG-SimPlus simulates
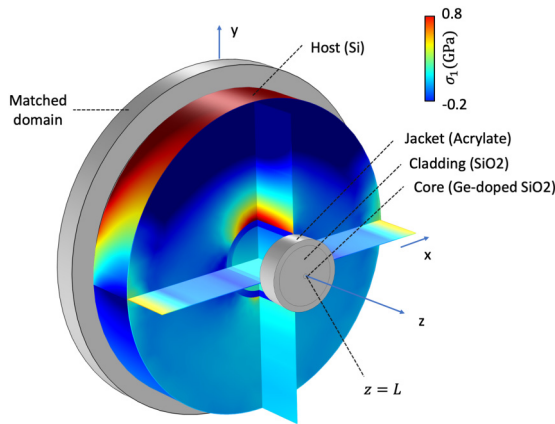

FIG. 3. Computed stress distribution in a $z = L = 200$ μm segment of an embedded FBG sensor for materials listed in Table I. An arbitrary deformation is here simulated by the application of a boundary force of $f_y = -10$ GN m^{-2} on the $y > 0$ segment of $\partial \Omega_{H,\infty}$. To mechanically simulate the host bulk, external (infinite) subdomains Ω_∞ with suitable scaling properties are considered. The outmost boundaries are constrained to suppress irrelevant (rigid) degrees of freedom with all other boundaries conditioned to deform freely.

TABLE II. Computational domain configurations. Data is extracted from the 3D domains to 1D along path S.

Setup	Subdomains	Path S on
1	$\Omega_\infty, \Omega_H, \Omega_J, \Omega_{CL}, \Omega_C$	Core
2	$\Omega_\infty, \Omega_H, \Omega_{CL}, \Omega_C$	Core
3	$\Omega_\infty, \Omega_H, \Omega_J, \Omega_{CL}$	Cladding
4	$\Omega_\infty, \Omega_H,$	Host

one-dimensional (1D) solutions, using our three-dimensional (3D) stress and strain results, corresponding to each of the listed configurations, necessitates the definition of a path S along which data can be extracted one dimensionally. The results are displayed in Fig. 4. The path S on the fiber is exemplified in Fig. 5, where the solutions are extracted (interpolated between the pertinent mesh points). This 1D output data will be used as input data into the FBG simulator.

At a point on the surface, stress at a surface point may be decomposed into normal components (perpendicular to the surface corresponding to compression or tension), and into components parallel to the surface (shear stress). Here, σ_{ii}
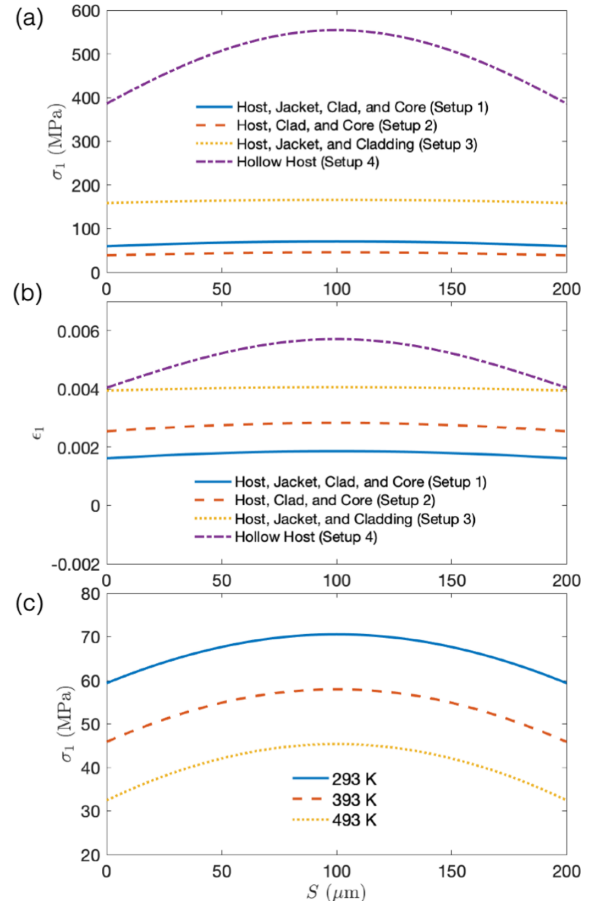

FIG. 4. Computed stress and strain as functions of material properties and temperature extracted from the 3D solutions along path S defined on subdomains listed in Table II. The principal stress component (a), (c) and strain component (b) exhibit significant variations as a function of core and cladding materials (a), (b) and as a function of temperature (c).
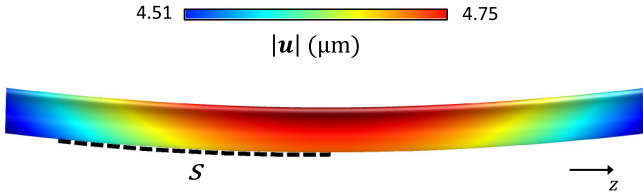
FIG. 5. Computed total displacement visualized for the fiber core only. The displacement has been scaled by a factor of 20 to visualize the core curvature. The embedded fiber has a length of 200 μm. FBG simulator input data is extracted along a path S on the core, shown here arbitrarily.

give the normal stress, while the off-diagonal components (σ_{ij}, $i \neq j$) describe the shear forces. As can be seen in Fig. 4, positive (negative) normal stress corresponds to tension (compression). The displayed principal stresses σ_i, or the eigenvalues of the stress tensor (i.e., $\boldsymbol{\sigma} = \sigma_i \boldsymbol{e}_i \boldsymbol{e}_i$), indicate that, in transferring stress from the host to the core of the fiber, significant differences can arise as a result of different material type and thickness of the cladding (and jacket or other FBG layers). From the above relations, the strain can be computed which in turn can be used to solve for the stress field. From the real part of the computed displacement field $\boldsymbol{u}$ components, we obtain a total deformation $(u_r^2 + v_r^2 + w_r^2)^{1/2}$, as visualized in Fig. 5.

C. Strain contributions

For an accurate model, the various contributions to the strain need to be identified and accounted for. These contributions can lead to residual stresses from the embedding process (e.g., if the fiber is glued to a surface or plotted in a matrix), stresses due to thermal changes, and stresses due to external forces applied to the combined structure. Other processes contributing to inelastic strain such as plasticity, viscoplasticity, and creep (cold flow) deformation may have to be considered, e.g., for harsh environment applications. Similarly, contribution to strain from electrostrictive effect, hygroscopic swelling, and radiation damage can become significant in specific applications.

In an otherwise undisturbed FBG encased in an outer layer, for example via immersion into a polymer or liquid mix followed by drying or curing, significant initial (inelastic) strain $\boldsymbol{\varepsilon}_i$ can develop, thus contributing further to total strain. From the detection point of view, only sensing signals generated by transformation of the medium with reference to this initial strain state is of interest. Inclusion of an initial stress contribution changes the generalized Hooke's law to $\boldsymbol{\sigma} - \boldsymbol{\sigma}_i = \boldsymbol{C} : (\boldsymbol{\varepsilon} - \boldsymbol{\varepsilon}_i)$. By assuming a reasonable form of $\boldsymbol{\varepsilon}_i$, for example, by a series of before and after embedding measurements, we may model the effects of drying or curing a matrix medium.

With the above description and formulation of the mechanical model, we now seek to determine the shift in the guided mode field distribution and further in the wavelength $\delta\lambda_B$.

D. Optical modeling consideration

1. Subdomain dielectric properties

Optically, the fiber comprises a core of index n_C, a cladding of index n_{CL}, and a multilayer protective layer or jacket

TABLE III. Model subdomain optical properties.

Subdomain	Material	$n\|_{\lambda=1550 \text{ nm}}$	ξ ($\times 10^{-6}$) (K^{-1})
Ω_C	Ge-doped SiO$_2$	1.4457	10.5
Ω_{CL}	SiO$_2$	1.4378	8.6
Ω_J	Acrylate	1.5	
Ω_H	Si	3.48	
Ω_∞	Matched	Matched	Matched

(typically including an inner rubbery layer surrounded by a more rigid layer such as polyimide or acrylate) of index n_J. These make up the first three computational subdomains, over which the fields are sought. For clarity, we first briefly describe the optical properties of the involved materials in terms of the dielectric tensor ϵ, generally defined via

$$\boldsymbol{D}(\boldsymbol{r}, t) = \epsilon_0 \iint \epsilon(\boldsymbol{r} - \boldsymbol{r}', t - t') \boldsymbol{E}(\boldsymbol{r}', t') d^3\boldsymbol{r}' dt',$$

where $\boldsymbol{D}$ ($\boldsymbol{E}$) is the electric displacement (field). This general definition is used here to draw attention to the possibility of nonlocal effects. For example, in plasmonics and nanophotonics, nonlocal dielectric functions are sometimes necessary to account for spatial dispersion. In the presented model, for the specific class of materials, considered relevant to FBG sensing, the spatial dispersion is approximately negligible, i.e., a local dielectric function is assumed. Furthermore, in the spectral ranges of interest, the temporal dispersion is also negligible. Thus, in Fourier space $\epsilon(\boldsymbol{k}, \omega) \approx \epsilon$, for the momentum $\boldsymbol{k}$ and frequency ω ranges considered. Further, the dielectric function, being a second-rank tensor, is written as $D_i = \epsilon_{ij} E_j$, $i, j = 1, 2, 3$, which will be quantified in the section below when discussing stress-induced mode shift. The specific optical properties used for each subdomain Ω in our simulations are given in Table III.

In a closing remark, we also note that often the specific index modulation profile may not be known. If the refractive index modulation spatial dependence $n(x, y, z) = \sqrt{\epsilon}$ is known or can be measured, further possibilities may be explored. For 1D field propagation (in the z direction), $\nabla_z \boldsymbol{E} - \mu\epsilon(z)\boldsymbol{E}_{tt} = 0$, which may be a reasonable approximation for an SMF, the analytical expression $\epsilon(z) = \bar{n}^2 + Z(z)$, where $\bar{n}$ is the average index, and Z is a periodic function in z, may be used in the computational domain, or be Fourier expanded and used in coupled-mode calculations.

2. Computational ray tracing

As noted above, the large ratio $N\Lambda/\lambda$ creates a modeling challenge for effective computation of field propagation in arbitrarily warped grating lines. To assess suitable approaches to the optical modeling in Ω_C, Ω_{CL}, and Ω_J subdomains, it is worth considering ray tracing using geometric optics, which offers an advantage for large length-scale simulations, even in the case of a Bragg grating. Though in general, ray tracing and geometric optics ignore the phase evolution of the field, in a more advanced calculation, the time t and position x variation of the optical field E associated with each ray can indeed be calculated. Therefore, the phase of a ray can be accounted for (along with the ray intensity, polarization, and
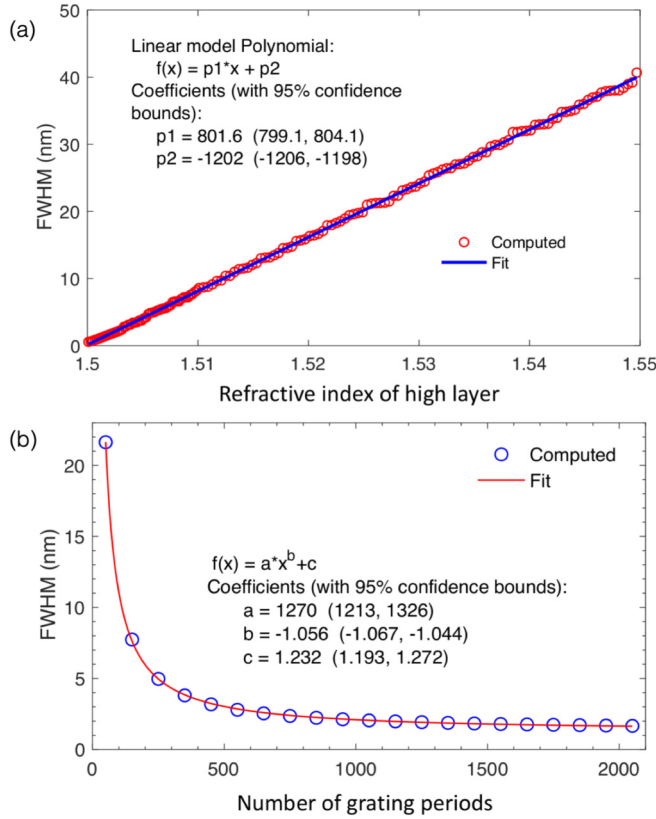
FIG. 6. Computed Bragg spectral properties using ray tracing. Optical properties used are listed in Table III.

FIG. 7. Curvature-induced redistribution of the z component of the first mode field E_z in a SMF. Here, a radius of curvature of $\rho = 200$ mm essentially yields the same core confinement as an undeformed fiber. Optical properties used are listed in Table III, and $T = T_i = 293$ K. The radius of curvature of $\rho = 5.84$ mm was selected for its correspondence to the max deformation visualized in Fig. 5.

path length) and employed to determine various interference patterns such as those arising in an interferometer or from interference between the reflected waves at the interfaces of the FBG.

The validity of ray tracing hinges upon the waveguide diameter ($2R_C$) satisfying $R_C \gg \lambda$, which is clearly not satisfied in a SMF, where $R_C \sim \lambda$. Additionally, incorporation of the spatial modulation of the dielectric function in an FBG with arbitrarily deformed cross-sectional geometry is not trivial. In fact, it is quite feasible to develop a 3D ray tracing model that yields the spectral response of a Bragg grating built upon an optical medium (of proper waveguide size compared to λ) by lumping N ($\sim 10^3$) Fresnel reflections at the boundaries of simple modulation profiles (Cartesian high-low transitions similar to those developed for optical filter design) into a single boundary. For fields of vacuum wavelength λ to reflect and interfere constructively, the optical thickness of the layers $n_H t_H$ and $n_L t_L$ are constrained to $\lambda/4$ to yield useful photonic bandwidth, $\Delta\lambda$, for practical sensing [31]. However, accounting for nonuniform axial and radial displacement that, for example, warp the grating grooves is not amenable to modeling with ray tracing. For slow curvature or straight waveguides, the approach is particularly useful for FBG design purposes. Such designs often consider the FWHM of the signal, and/or how $\Delta n = n_H - n_L$ may vary with the number of grooves as a merit. Figure 6 shows the result of simulating the Bragg spectral properties using ray tracing in a multimode fiber medium (with $R_C \gg \lambda$) containing a Bragg grating region made up of $N = 2000$ Fresnel transitions. As
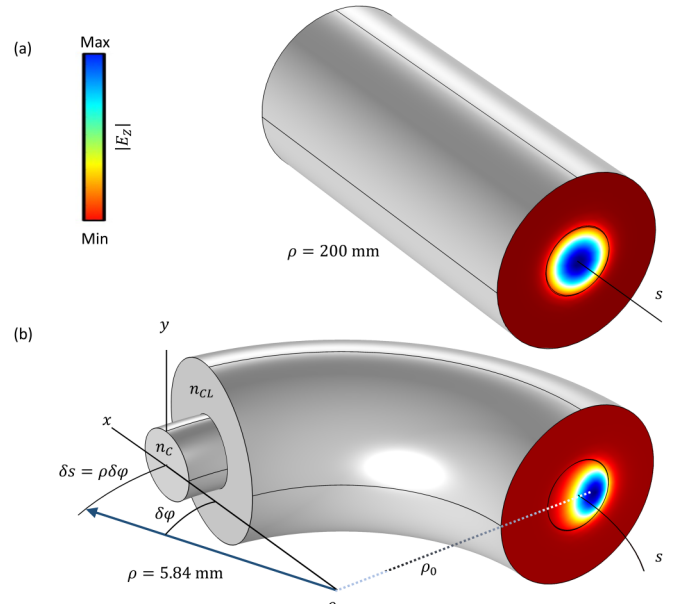
can be seen, the FWHM increases with Δn and decreases with N. Here, computational ray tracing [32] was employed to gain insight and validate the predicted shift from the FBG simulator.

3. Curvature-induced mode shift

When the optical subdomains (Ω_C, Ω_{CL}, and Ω_J) deform, two effects are to be considered: first, a purely geometric effect in which the optical properties of the deformed material is assumed unchanged; and second, a mechanical modification of the optical properties of the deformed waveguide. These effects occur regardless of whether the waveguide hosts a Bragg domain or not. With reference to Fig. 7, scattering losses associated with purely geometric effects on the guided mode may be studied. Prior to the computational determination of the deformed fiber eigenmodes, it is illuminating to point out that the radial and azimuthal wave-vector components in the bent fiber can be approximated in terms of the curvature parameters [25]. Writing the bent eigenmode u in the form

$$u(x, y, g, t) = p_m(x, y) e^{i(\omega t - \beta_m g)},$$

where p_m is the mth mode profile, and g and β_m depend on the deformation of the fiber. For an undeformed fiber, $g = z$, and the propagation constant $\beta_m = k_0 n_{\text{eff},m}$, expressed usually in terms of an effective index $n_{\text{eff},m}$, while for a deformed fiber with a simple curvature defined by the radius ρ, $g = \rho_0 \varphi$ with ρ_0 denoting the average mode radius (not at the center of the core), as indicated in Fig. 7. Thus, the eigenvalues β_m change to $\beta_m \rho_0$ leading to new values for n_{eff}.

To determine the bending-induced optical mode disturbance, we compute the electric field of a SMF by solving the field eigenvalue equation $\nabla \times \nabla \times \boldsymbol{E} = k_0^2 \epsilon_\Omega \boldsymbol{E}$, where $k_0 = 2\pi/\lambda$, noting that an effective mode index (defined as the ratio of the wave number and the free space wave number),

$$n_{\mathrm{eff}} = k/k_0 < n_\Omega = n_C = n_{\mathrm{GeSiO_2}} = 1.4457,$$

is assumed to allow a propagating mode confined to Ω_C. To compute the eigenmodes, we here consider an axisymmetric 2D computational domain corresponding to a cross section of the model in Fig. 7 or in Fig. 3, i.e., with a unit normal $\boldsymbol{z}$. Here, a perfect magnetic conductor boundary condition, i.e., $\boldsymbol{n} \times \boldsymbol{H} = 0$, is imposed on $\partial\Omega_{CL,J}$ to emulate the extent of the optically conductive regions (see Fig. 1). The eigenvalue equation is solved for Ω_C and Ω_{CL} using a maximum mesh element size of 14 μm and a minimum element size of 52 nm. For $\lambda = 1550$ nm, primarily single modes are allowed at an effective index of $n_{\mathrm{eff}} = 1.4444$. For $T = T_i$, the results are shown in Fig. 7 for a single mode. Higher modes that can be excited for larger waveguide diameters (e.g., in multimode fiber) exhibit similar shifts with reduced core confinement (coupling of the light into the cladding). The solutions provide insight into the degree of mode shifts, albeit direct inclusion of a deformable Bragg structure is not feasible in the 2D model and is nontrivial in 3D. Furthermore, this formulation does not include photoelastic contribution to the mode properties, that is, it does not account for the stress-induced modification of the core refractive index.

E. Photoelastic contribution

Any induced stress σ_{kl} (strain ε_{kl}) alters the indices of refraction Δn_{ij} of the subdomain materials due to changes in the material density and polarizability. The resulting photoelasticity (or piezo-optic effect), is expressed via the stress-optic q_{ijkl} (also known as the piezo-optic π_{ijkl}) tensor. Indices of refraction may also be related to strain through the strain-optic (also known as the elasto-optic p_{ijkl}) tensor. For the optically most relevant material domains (Ω_C, Ω_{CL}) with unstrained index n_Ω at fixed $T = T_i$, an induced stress changes the index as

$$\Delta n_{ij} = n_{ij} - n_\Omega I_{ij} = q_{ijkl}\sigma_{kl}, \tag{1}$$

where $\boldsymbol{I}$ is the identity tensor. We write the index variation for the fiber under stress as

$$\Delta\boldsymbol{n}(\boldsymbol{\sigma}) = \begin{pmatrix} \Delta n_1 \\ \Delta n_2 \\ \Delta n_3 \end{pmatrix} = \begin{pmatrix} q_{11} & q_{12} & q_{13} \\ q_{21} & q_{22} & q_{23} \\ q_{31} & q_{32} & q_{33} \end{pmatrix} \begin{pmatrix} \sigma_1 \\ \sigma_2 \\ \sigma_3 \end{pmatrix}, \tag{2}$$

where the coefficients q_{ij} with $i, j = 1, 2, 3$ or $= x, y, z$ [note $q_{44} = (q_{11} - q_{12})/2$; see Eq. (A1)], characterize the connection between the principal refractive indices and stress. Via the stress and strain relationship, Δn_{ij} may also be expressed in terms of strain. In the case of an isotropic material, the elasto-optic tensor may be expressed as in Eq. (A1). All elasto-optic coefficients p_{ij} presented are dimensionless. In terms of strains $\Delta\boldsymbol{n}(\boldsymbol{\varepsilon})|_i = p_{ij}\varepsilon_j$. Assuming an initially undeformed medium, where the core and cladding materials are optically isotropic, only two components are unique. Then numerically, we can use the photoelasticity effect investigated
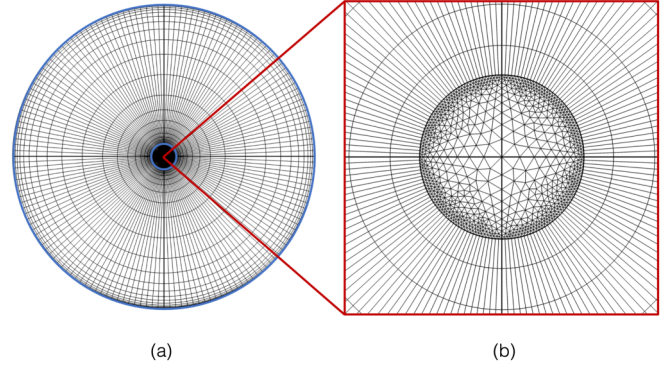

FIG. 8. Meshing of the subdomains for the computational analysis of the optical states of the stratified medium. The mesh shown corresponds to Ω_C and Ω_{CL}, indicated respectively by the inner and outer blue circles (a). The core and cladding are shown (a), with a mapped maximum mesh element size of 14 μm and minimum element size of 52 nm. A close-up of the free tetrahedral mesh that composes a small segment of the core center (b) is also visualized with a maximum mesh element size of 7 μm and a minimum element size of 14 nm.

by Erba and Dovesi [33] and Detraux and Gonze [34] with values reported in terms of (Pockels') tensor components p_{ij}, which can be expressed in terms of the parallel and perpendicular changes of the index of refraction with stress $Q_\parallel$ and $Q_\perp$, respectively. Taking the core to be α quartz, then $p_{11} = 0.13$ and $p_{12} = 0.28$ as reported by Davis and Hayden [35] and Bach and Neuroth [36], we obtain

$$Q_\parallel = -\frac{n_\Omega^3}{2} q_{11}$$
$$= -\left(\frac{n_\Omega^3}{2E_\Omega}\right)(p_{11} - 2\nu_\Omega p_{12}) = -0.65 \text{ B},$$
$$Q_\perp = -\frac{n_\Omega^3}{2} q_{12}$$
$$= \left(\frac{n_\Omega^3}{2E_\Omega}\right)[-\nu_\Omega p_{11} + (1 - \nu_\Omega)p_{12}] = -4.2 \text{ B},$$

where the units are given in Brewster (1 B $= 10^{-12}$ Pa^{-1}). Note that the reported values are for measurements and calculations at specific wavelengths assumed, and slight spectral variations are reported for these values. We also note that $q_{11} = q_{22} = q_{33}$ while $q_{12} = q_{21} = q_{13} = q_{31} = q_{23} = q_{32}$. With computed $\boldsymbol{\sigma}$, we can thus map the spatial variations of $\Delta\boldsymbol{n}$. To this end, to solve the Navier and stress-strain equations to obtain the shift Δn, and the eigenvalue equation for the electric field to obtain the guided mode, we consider a long fiber, and to reduce the computational burden, we assume that strain components perpendicular to the crosssectional plane ($\boldsymbol{e}_1$, $\boldsymbol{e}_2$) are negligible, in which case $\varepsilon_{13} = \varepsilon_{23} = \varepsilon_{33} \approx 0$ (i.e., plane strain). Here, care must be applied for the meshing when considering a symmetrically embedded fiber under the condition of no force but elevated T. To avoid accumulation of numerical error which can show up as changes in Δn_i, a highly symmetric meshing must be invoked, as shown in Fig. 8.

For the applied boundary force $f_y = -10$ [GN m^{-2}] (as in Fig. 9), the results are shown in columns (c) and (d) of
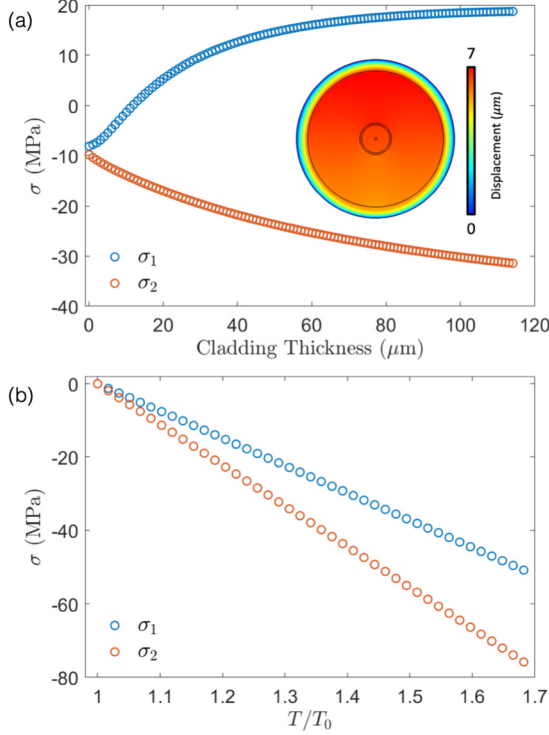
FIG. 9. The variation of fiber core principal stress as a function of cladding material and thickness (a) and temperature (b). An arbitrary deformation is here simulated by the application of a boundary force of $f_y = -10$ (GN m^{-2}) (top), and elevated temperature with no applied force (bottom).
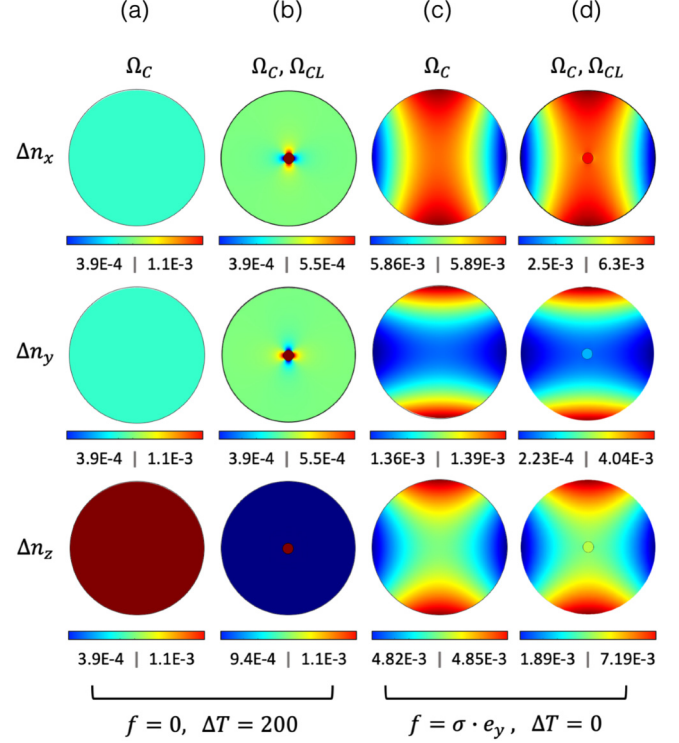

FIG. 10. Refractive index components resulting from induced stress due to thermoelastic [columns (a) and (b)], and elastic [columns (c) and (d)] contributions.

Fig. 10, where significant variations in the components of $\Delta \boldsymbol{n}$ are observed across Ω_C and Ω_{CL}. The induced stress and the consequent index variations shown in Fig. 10 cause a variation in the guided mode property. We then solve for the field eigenmode to determine the guided mode properties. The results are shown in Fig. 11, where a significant mode field redistribution is observed. Such modal changes in the grating region consistent with the refractive index variation contribute to the sensor output change.

An effective elasto-optic coefficient may be developed for a homogeneous and isotropic strain [37]:

$$p_e = (n^2/2)[p_{12} - \nu(p_{11} + p_{12})]. \tag{3}$$

Thus, for a strain-induced Bragg shift, where $\bar{\varepsilon}_s$ indicates the true strain averaged along the finite path S as depicted in Fig. 5,

$$\Delta \lambda_B^{T_i}(\varepsilon) = \lambda_B (1 - p_e) \bar{\varepsilon}_s. \tag{4}$$

F. Temperature contribution

1. Thermoelastic effect

To incorporate the contributions to λ_B from thermoelastic [38] effects, i.e., temperature-driven stresses, and from thermo-optic effects, i.e., temperature induced changes in n_C and n_{CL}, we first note the inelastic contribution of temperature $\boldsymbol{\varepsilon}^T$ to the total strain $\boldsymbol{\varepsilon}_t = \boldsymbol{\varepsilon} + \boldsymbol{\varepsilon}^T$. For $T \neq T_0$, generally the layers in Fig. 1 respond by changing their volumes, and since FBG sensors can often be physically constrained due

to embedding or attachment, significant stresses can develop even for moderate ΔT. The thermal strain $\boldsymbol{\varepsilon}^T$, generating stress-free deformations, accounts for the volume changes. To account for the temperature changes, we note that given the diameter of typical SMFs ($\sim$10 μm), the cross-sectional thermal transport can occur at times $t < 1\ \mu$s so that in some applications, one may safely assume a uniform cross-sectional temperature. Nevertheless, in fast thermal cycling, transient effects can be significant, as may be shown by solving the heat diffusion equation. For nonuniform heating, neglecting heat flux by radiation, $\boldsymbol{\Phi}_r$ (non-negligible at high T), in Fig. 1, we obtain $T(\boldsymbol{r}, t)$ by solving the heat diffusion equation:

$$\rho_\Omega C_\Omega \boldsymbol{u} \cdot \boldsymbol{\nabla} T - \boldsymbol{\nabla} \cdot k_\Omega \boldsymbol{\nabla} T + \rho_\Omega C_\Omega T_t = \sum_i Q_i, \tag{5}$$
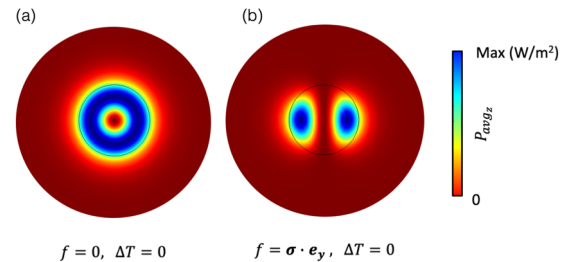

FIG. 11. Computed field changes of the single mode of an SMF. The unperturbed mode (a) exhibits significant elastic mode field changes (b) in response to f.
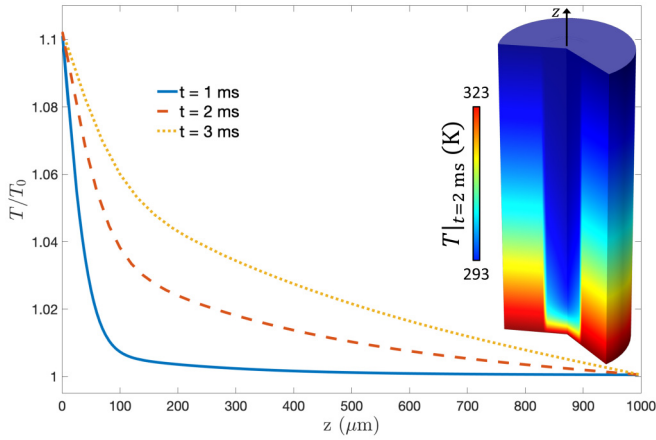
FIG. 12. Temperature distribution in an embedded fiber segment of length 1000 μm. The core, cladding, jacket, and the embedding host subdomains are made of pure SiO$_2$ assumed close to Ge-doped SiO$_2$, pure SiO$_2$, acrylate, and Si, respectively. The plot displays the temperature on the z axis at the center of the fiber core.
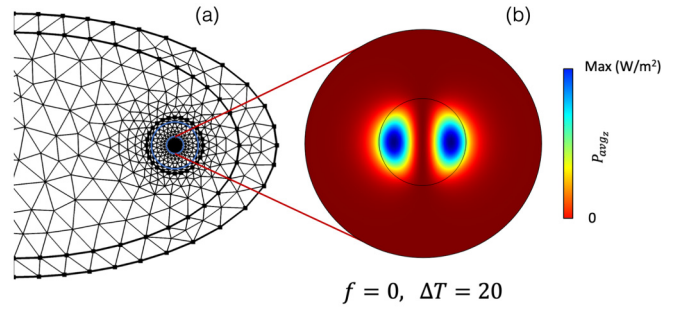

FIG. 13. Birefringent optical mode changes (b) as a result of an asymmetrical geometry (a) and a uniform $\Delta T = 20$ K.

where ρ_Ω, C_Ω, and k_Ω are, respectively, the density, heat capacity, and thermal conductivity of subdomain d, while Q_i is the ith source term (e.g., due to conduction from the host or absorption of radiation by the host, etc.). In general, k_Ω is a symmetric positive-definite second-order tensor, especially for multilayer and composite material domains. For small convective heat transport as in the present case, and assuming a thermal insulating boundary condition $-\boldsymbol{n} \cdot \nabla T = 0$ along the boundary $\partial\Omega_{H,\infty}$, the result is shown in Fig. 12. As can be seen, heat evolution along a 1-mm-long system occurs at approximately millisecond timescales. It is worth noting that the thermoelastic effect in the various subdomains generates a source term $-\boldsymbol{\alpha}T : d\boldsymbol{\sigma}/dt$, where $\boldsymbol{\alpha}$ is the thermal expansion coefficient, and d/dt is the time derivative operator in the material frame [39]. Transient or rapid changes in stress (e.g., high-frequency vibrations) may generate significant heat. Here, in the computation of optical mode changes, the temperature changes in subdomains translate to mechanical loads and thus subdomain expansion. For smaller domains, thermal expansion that leads to stress generation is therefore here taken into account by a single temperature assignment to the domains, referenced to an initial temperature ($T_i = 293$ K).

With ΔT computed for a given domain, the contribution to strain can be written as

$$\boldsymbol{\varepsilon}_{ij}^T = \alpha_{ij}(T)\Delta T + O[(\Delta T)^2], \tag{6}$$

where α_{ij} are the thermal expansion coefficient components. Numerically, $\alpha \sim (10^{-7}\text{–}10^{-5})$ K^{-1}, e.g., $\alpha_{\text{SiO}_2} = 5.5 \times 10^{-7}$ K^{-1}, as summarized in Table IV. Thus, in the linear regime

$$\sigma_{ij} = C_{ijkl}(\varepsilon_{kl} - \alpha_{kl}\Delta T). $$

By taking into account Eq. (6), when computing the displacements $\boldsymbol{u}$, we obtain the results in Fig. 13 for the thermoelastic optical mode splitting, assuming $\Delta T = 20$ K. To obtain the pronounced mode splitting observed, we assumed an asymmetric placement of the core-cladding-jacket domains with respect to the host thus creating a nonuniform displacement leading to large stress formation. This result provides a direct method to design extremely sensitive thermal BFG sensors by optimizing differential thermal expansions.

Having computed σ with and without contribution from thermal expansion, we compare the stress provided by analytically augmenting the Bragg shift equation. Accounting for temperatures $T \neq T_i$, and assuming a uniform heating over moderate temperature ranges for isotropic materials, we have $\boldsymbol{\varepsilon}_{ij}^T \approx \alpha\Delta T$. Thus, the Bragg shift is now written as

$$\Delta\lambda_B(\varepsilon, T) = \Delta\lambda_B^{T_i}(\varepsilon) + \alpha_f\overline{\Delta T}_s, \tag{7}$$

where α_f is the thermal expansion coefficient of the fiber. The thermal expansion of the fiber is often in reference to that of the cladding due to its large volume and mass relative to the core, especially in a SMF implementation. When $\alpha_C > \alpha_{CL}$, the thermal expansion of the core is restricted and appears as compressed relative to its unbound state. The difference in thermal expansion of the core and cladding is an optically relevant issue in which an analytical model has been proposed [40].

TABLE IV. Model subdomain thermal properties.

Sub-domain	Material	C [J/(kg K)]	k [W/(m K)]	α ($\times10^{-6}$)(K^{-1})
Ω_C	Ge-doped SiO$_2$			2
Ω_{CL}	SiO$_2$	703	1.4	0.55
Ω_J	Acrylate	1470	0.18	70
Ω_H	Si	700	130	2.6
Ω_∞	Matched	Matched	Matched	Matched

2. Thermo-optic effect

Temperature changes also induce variations in the refractive indices (n) of the materials (thermo-optic effect), which can be described via a second-rank symmetric tensor (since T is scalar). At frequency ω, the dielectric function of a subdomain, here assumed isotropic, is $\epsilon_{ij}(\omega, T) = \epsilon(T)$ and thus $d\epsilon/dT = 2\xi n$, where $\xi = dn/dT$ is the thermo-optic coefficient of the medium. When $T \neq T_i$, thermo-optic effects may have to be considered since

$$n(T) = n(T_i) + \xi \Delta T. \tag{8}$$

For example, for the core material $\xi_{\text{Ge-doped SiO}_2} \sim 1.05 \times 10^{-5}$ K^{-1} and thus a relatively large thermo-optical effect is expected for moderate T in comparison to thermal expansion. For an isolated fiber (no embedding medium), the modified Bragg shift is written as

$$\Delta\lambda_B(\varepsilon, T) = \Delta\lambda_B^{T_i}(\varepsilon) + (\alpha_f + \xi)\overline{\Delta T}_s, \tag{9}$$

where α_f and ξ are the (linear) thermal expansion coefficient and the thermo-optic coefficient, respectively, of the fiber core material. In Eq. (4) and Eq. (9), the index S denotes the path along which ε_s and ΔT are averaged as shown in Fig. 5, for example.

Another consideration arises when a fiber is embedded within a host material. In this case Eq. (9) must be amended to account for the thermal expansion coefficient of the host relative to the fiber [41]:

$$\begin{aligned} &\Delta\lambda_B(\varepsilon, T) \\ &= \Delta\lambda_B^{T_i}(\varepsilon) + [\alpha_f + \xi + (1-p_e)(\alpha_h - \alpha_f)]\overline{\Delta T}_s, \end{aligned} \tag{10}$$

where α_h is the thermal expansion coefficient of the host. In the case of an embedded fiber for a sufficiently large host, the thermal expansion of the fiber core, cladding, and jacket are relatively small in comparison to that of the host. In our modified FBG simulator, FBG-SimPlus V1.0, we have implemented Eq. (10) to allow simulation of embedded grating scenarios. More general cases in which the material properties exhibit significant T dependence such that, e.g., $E = E(T)$, or $\alpha = \alpha(T)$, etc., are not considered here.

III. EXPERIMENTAL MEASUREMENTS OF λ_B

To demonstrate the viability of the presented semianalytical method and FBG-SimPlus for calculating the Bragg shift under arbitrary external stimuli, we carried out measurements on an FBG implemented in a single-mode step-index fiber (Technica FBG sensor [42]) with optical conductivity at wavelengths in 1460–1620 nm (± 0.5 tolerance). These sensors are typically fabricated via exposing the core of the fiber to a UV radiation (e.g., from an excimer laser) interference pattern, which owing to the Ge doping of the SiO$_2$ core making it photosensitive, permanently modulate the core index of refraction. The fibers are acrylate coated, and incorporate nonapodized (uniform), 2-mm-long FBGs of overall diameter 125 μm with a central wavelength of $\lambda_{b_0} = 1549.6$ nm at $T_0 = 0\,^\circ$C. The sensors exhibit good temperature and strain linearity with stable output for temperatures up to $T = 300\,^\circ$C. In a basic setup, a beam from an infrared laser (e.g., a tunable semiconductor laser), with a wavelength typically in
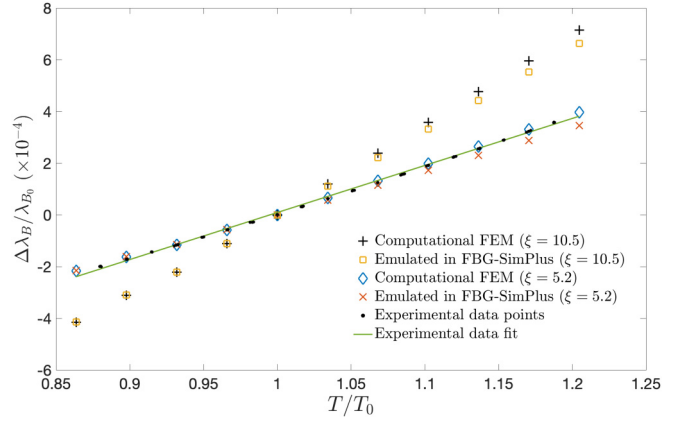

FIG. 14. Validation of FBG-SimPlus temperature functionality with experimental measurement of the relative Bragg shift. The straight FBG, subjected to a variation in temperature, responds with a Bragg shift.

the telecom C band (telecommunication's conventional band: 1530–1565 nm), is coupled into the fiber via a fiber coupler and the reflected light is routed to a photodetector via an optical circulator (a three-port optical channel). The source can be broadband with a filter (e.g., a tunable Fabry-Perot or via a dispersive medium) for spectral scanning. For standard measurements, these operations can be achieved using an optical interrogator, an integrated optical system for wavelength analysis of FBG output. Here, we carried out a series of measurements on our FBGs at ambient and elevated temperatures using an (four-channel) interrogator (FAZT-14G [43]). The FBG output is analyzed by exploring the full reflected spectrum or by detecting and monitoring the peak spectral position (source laser linewidth = 20 MHz). Within the 39.2 nm spectral window 1529–1568.2 nm of the interrogator, the wavelength increments $\Delta\lambda$ have to be sufficiently small to recover the narrow-width peak. The reflection bandwidth of the employed fibers is 0.1–0.8 nm with better than 70% reflectivity. Here, the wavelength resolution is set at $\Delta\lambda = 1$ pm with an absolute accuracy of <1 pm, and precision of <0.1 pm, which is maintained by referencing a gas cell and a Mach-Zehnder interferometer.

The experiments were carried out in a chamber featuring environmental control. At elevated steady-state chamber temperatures, for a fiber mounted to be straight, we acquired spectral data to be analyzed and compared with the computational results for the stress, strain, and initial temperature information, which were extracted along path S (Fig. 5) of the fiber and presented to FBG-SimPlus as input data. The results are shown in Fig. 14, where two simulation scenarios using the computational input data are displayed. The first scenario involves temperature control via the computational model of Fig. 3, implemented using FEM, to simulate thermal expansion of the core, cladding, jacket, and the host of the FBG sensor implementation. In this case, computational stress, strain, and temperature information are imported into FBG-SimPlus, that is, the simulator is run with no temperature emulation feature enabled and the Bragg shift is then calculated. In the second scenario, the mechanical response of the system (Fig. 3) is obtained via the computational model

using FEM. In this case, within the FBG-SimPlus simulator, the user can simulate a temperature perturbation. From here temperature is emulated within FBG-SimPlus to account for the photoelastic effect due to thermal strain, effect of thermal expansion, and the thermo-optic effect for various temperature contribution scenarios. As can be seen from Fig. 14, FBG-SimPlus provides good agreement with experimental results. Here, ξ, while not treated as a free parameter, can be varied iteratively over a reasonable range for better consistency. The lack of a consistent set of material properties for doped fiber core implies that ξ may be varied within a range of plausible values reported [44]. Similarly, the mechanical properties (E, ν) of our fiber into which the FBG is written are subject to some variation.

IV. CONCLUSIONS

In conclusion, the presented computational approach in conjunction with the modified version of the semianalytical calculation was shown to produce good agreement with our experimental results. Thus, the effects of stress, strain, and temperature on the photonic eigenmodes of a waveguide embedded arbitrarily in a stratified material can be investigated following the presented method. In doing so, we also implemented a temperature dependence in FBG-SimPlus. The simulated response of an FBG sensor is accounted for without any specific assumption or constraints on the material or geometric properties of the domains. The presented model accounted for both photoelastically induced birefringence, and for thermal expansion induced mode splitting. The new version of the FBG simulation code allows the analysis of temperature contribution via both the photoelastic and thermo-optical changes, as an additional simulation feature. Our study with the cantilever subjected to deformation and temperature variations allowed analysis in the context of the improved functionality for published FBG simulation code. The developed computational model proved highly flexible with respect to parameter variations that correspond to geometric, material, and stimuli changes, opening the path for envisioning new applications. For example, in security-related applications, FBG designs that prevent the duplication of the sensor response are desired. In the development of such FBG sensors—with a hard-to-duplicate response—further intricate FBG designs may be considered, following the presented work here and using more elaborate dielectric tensors ϵ_{ij}. From our results, we conclude that with sufficient computational power, the wave propagation modeled via FDTD coupled with finite elements calculation of the model deformation and thermal considerations will enable a complete modeling platform. Though, here both the mechanical and optical processes were considered within linear regimes and for uniform Bragg periodicities, nonlinear mechanical effects such as geometric nonlinearity due to large deformations, and nonlinear optical effects such as the Kerr nonlinearity or contributions from nonlinear index response at higher pulse energies, as well as, chirped, apodized, or other nonuniform Bragg forms may be treated similarly.

The Department of Energy will provide public access to these results of federally sponsored research in accordance with the DOE Public Access Plan [45].

APPENDIX A: TENSOR QUANTITIES

We define the elasto-optic or stress-optic tensor M as

$$M = \begin{bmatrix} m_{11} & m_{12} & m_{12} & 0 & 0 & 0 \\ m_{12} & m_{11} & m_{12} & 0 & 0 & 0 \\ m_{12} & m_{12} & m_{11} & 0 & 0 & 0 \\ 0 & 0 & 0 & m_{44} & 0 & 0 \\ 0 & 0 & 0 & 0 & m_{44} & 0 \\ 0 & 0 & 0 & 0 & 0 & m_{44} \end{bmatrix}, \quad \text{(A1)}$$

where m_{ij} may either represent p_{ij} of the fourth-rank elasto-optic tensor or q_{ij} of the stress-optic tensor depending on whether solving for a supplied strain or stress, respectively.

APPENDIX B: COMPUTATIONAL CONSIDERATIONS

Using a desktop computer with 16 GB of 2133 MHz memory and a Core i5-6600 quad-core processor with a clock speed of 3.30 GHz, a single FE simulation time t_{sim} is typically in the range $\sim t_{\text{sim}} \sim (3$–$900)$ s, when solving one or multiple PDEs, shown in Fig. 1. In the simulation, the mesh resolution δM, adjusted by varying the smallest and largest element sizes, and the specific PDEs and their boundary conditions solved affect t_{sim}. The results displayed in Fig. 14 represent a multistep processing of data. In one instance, for a cylindrical multilayered model, the stress and strain information is calculated at a given but fixed temperature via a $t_{\text{sim}} = 3$ s simulation (solution convergence). The results are then processed via FBG-SimPlus using one of two scenarios that are outlined in Sec. III. Each scenario roughly requires $t_{\text{sim}} = 30$ s.

[1] N. K. Efremidis, N. S. Nye, and D. N. Christodoulides, Exact bidirectional X-wave solutions in fiber Bragg gratings, Phys. Rev. A **96**, 043820 (2017).

[2] A. Kitagawa, and J. Sakai, Bloch theorem in cylindrical coordinates and its application to a Bragg fiber, Phys. Rev. A **80**, 033802 (2009).

[3] S. V. Raja, A. Govindarajan, A. Mahalingam, and M. Lakshmanan, Tailoring inhomogeneous $\mathcal{PT}$-symmetric fiber-Bragg-grating spectra, Phys. Rev. A **101**, 033814 (2020).

[4] C. N. Alexeyev, B. P. Lapin, G. Milione, and M. A. Yavorsky, Localized topological states in Bragg multihelicoidal fibers with twist defects, Phys. Rev. A **93**, 063829 (2016).

[5] Y. P. Shapira and M. Horowitz, Propagation of quasisolitons in a fiber Bragg grating written in a slow saturable fiber amplifier, Phys. Rev. A **83**, 053803 (2011).

[6] S. Helsby, C. Corbari, M. Ibsen, P. Horak, and P. Kazansky, Fiber Bragg gratings for atom chips, Phys. Rev. A **75**, 013618 (2007).

[7] R.-K. Lee and Y. Lai, Amplitude-squeezed fiber-Bragg-grating solitons, Phys. Rev. A **69**, 021801 (2004).

[8] S. Koyama, H. Ishizawa, S. Hosoya, T. Kawamura, and S. Chino, Stress loading detection method using the FBG sensor for smart textile, J. Fiber Sci. Technol. **73**, 276 (2017).

[9] W. Luo, F. Xu, and Y. Q. Lu, Reconfigurable optical-force-drive chirp and delay line in micro- or nanofiber Bragg grating, Phys. Rev. A **91**, 053831 (2015).

[10] R. L. Stillwell, I. L. Liu, N. Harrison, M. Jaime, J. R. Jeffries, and N. P. Butch, Tricritical point of the f-electron antiferromagnet USb$_2$ driven by high magnetic fields, Phys. Rev. B **95**, 014414 (2017).

[11] R. Schonemann, S. Imajo, F. Weickert, J. Yan, D. G. Mandrus, Y. Takano, E. L. Brosha, P. F. S. Rosa, S. E. Nagler, K. Kindo, and M. Jaime, Thermal and magnetoelastic properties of α-RuCl$_3$ in the field-induced low-temperature states, Phys. Rev. B **102**, 214432 (2020).

[12] S. Correia, P. Antunes, E. Pecoraro, P. Lima, H. Varum, L. D. Carlos, R. A. Ferreira. and P. S. André, Optical fiber relative humidity sensor based on a FBG with a di-ureasil coating, Sensors **12**, 8847 (2012).

[13] L. Liu, H. Zhang, Q. Zhao, Y. Liu, and F. Li, Temperature-independent FBG pressure sensor with high sensitivity, Opt. Fiber Technol. **13**, 78 (2007).

[14] F. Le Kien and K. Hakuta, Motion of an atom in a weakly driven fiber-Bragg-grating cavity: Force, friction, and diffusion, Phys. Rev. A **81**, 063808 (2010).

[15] X. W. Ye, Y. H. Su, and J. P. Han, Structural health monitoring of civil infrastructure using optical fiber sensing technology: A comprehensive review, Sci. World J. **2014**, 652329 (2014).

[16] Q. Wu, Y. Okabe, and F. Yu, Ultrasonic structural health monitoring using fiber Bragg grating, Sensors **18**, 3395 (2018).

[17] H. Hu, S. Li, J. Wang, Y. Wang, and L. Zu, FBG-based real-time evaluation of transverse cracking in cross-ply laminates, Compos. Struct. **138**, 151 (2016).

[18] D. Tosi, E. Schena, C. Molardi, and S. Korganbayev, Fiber optic sensors for sub-centimeter spatially resolved measurements: Review and biomedical applications, Opt. Fiber Technol. **43**, 6 (2018).

[19] G. Allwood, G. Wild, and S. Hinckley, Optical fiber sensors in physical intrusion detection systems: A review, IEEE Sens. J. **16**, 5497 (2016).

[20] H. M. Hairi, T. Saktioto, S. Nafisah, M. Fadhali, R. Qindeel, P. P. Yupapin, and J. Ali, Multi-photons trapping stability within a fiber Bragg grating for quantum sensor use, Prog. Electromagn. Res. **2**, 1699 (2010).

[21] R. K. Lee and Y. Lai, Quantum theory of fibre Bragg grating solitons, J. Opt. B: Quantum Semiclassical Opt. **6**, S638 (2004).

[22] C. D. Macrae, K. Bongs, and M. Holynski, Optical frequency generation using fiber Bragg grating filters for applications in portable quantum sensing, Opt. Lett. **46**, 1257 (2021).

[23] O. Hassoon, M. Tarfoui, and A. El Malk, Numerical simulation of fiber Bragg grating spectrum for mode-delamination detection, World Acad. Scie., Eng. Technol. Int. J. Mech., Aerospace, Indust., Mechatronic Manufacturing Eng. **9**, 144 (2015).

[24] R. B. S. Dahanayake, Simulations of step-like Bragg gratings in silica fibers using COMSOL, Master's thesis. OhioLINK Electronic Theses and Dissertations Center, Doctoral dissertation, University of Akron, 2016.

[25] Allan W. Snyder, and John D. Love, *Optical Waveguide Theory* (Springer US, Boston, 1984).

[26] J. S. Witkowski and A. Grobelny, Ray tracing method in a 3D analysis of fiber-optic elements, Opt. Appl. **38**, 294 (2008).

[27] G. Pereira, M. McGugan, and L. Mikkelsen, FBG_Simul V1.0: Fibre Bragg grating signal simulation tool for finite element method models, SoftwareX **5**, 163 (2016).

[28] B. Frey, FBG-SimPlus V1.0. GitHub repository, 2021, https://github.com/benfrey/FBG-SimPlus.

[29] A. Shirazi-Adl, An interface continuous stress penalty formulation for the finite element analysis of composite media, Comput. Struct. **33**, 951 (1989).

[30] F. Loth, T. Kiel, K. Busch, and P. T. Kristensen, Surface roughness in finite element meshes, arXiv:2002.00894.

[31] The photonic stopband can be shown to be given by $R(N) = r_{N^-}^2/r_{N^+}^2$, where $r_{N^\pm} = 1 \pm \alpha\beta^{2N}$, with $\alpha = n_H^2/(n_t n_b)$, with $\beta = n_H/n_L$, while the bandwidth is given by $\Delta\lambda/\lambda = 4\arcsin[(\beta - 1)/(\beta + 1)/\pi]$.

[32] COMSOL Multiphysics v. 5.5, https://www.comsol.com.

[33] A. Erba, and R. Dovesi, Photoelasticity of crystals from theoretical simulations, Phys. Rev. B **88**, 045121 (2013).

[34] F. Detraux and X. Gonze, Photoelasticity of α-quartz from first principles, Phys. Rev. B **63**, 115118 (2001).

[35] Mark J. Davis and Joseph S. Hayden, Stress-optic measurements of SCHOTT laser glass, in *Solid State Lasers XXVIII: Technology and Devices* (SPIE, 2019), pp. 206–221.

[36] H. Bach and N. Neuroth, *The Properties of Optical Glass* (Springer, Berlin, 1998).

[37] J. S. Sirkis, Unified approach to phase-strain-temperature models for smart structure interferometric optical fiber sensors: Part 2, applications, Opt. Eng. **32**, 762 (1993).

[38] For convenience, here the term "thermo-elastic" is used to refer to both stress effects caused by thermal expansion as well as to damping that can generate heat.

[39] The material time differentiation is connected to the spatial frame as $d/dt = (\partial/\partial t) + \boldsymbol{v} \cdot \boldsymbol{\nabla}\beta$, where $\boldsymbol{v}$ is the velocity vector of the translational motion so that $\boldsymbol{v} \cdot \boldsymbol{\nabla}$ corresponds to the convected quantity of the subdomains via translational motion.

[40] M. Cavillon, P. D. Dragic, and J. Ballato, Additivity of the coefficient of thermal expansion in silicate optical fibers, Opt. Lett. **42**, 3650 (2017).

[41] S. Magne, S. Rougeault, Manuel M. Vilela, and P. Ferdinand, State-of-strain evaluation with fiber Bragg grating rosettes: Application to discrimination between strain and

temperature effects in fiber sensors, Appl. Opt. **36**, 9437 (1997).

[42] https://technicasa.com/

[43] Fazt Technology Inc., Model I4G Interrogator, https://femtosensing.com/fazt-i4g-interrogator/

[44] G. Ghosh, *Handbook of Optical Constants of Solids: Handbook of Thermo-Optic Coefficients of Optical Materials with Applications* (Academic, New York, 1998).

[45] http://energy.gov/downloads/doe-public-access-plan